Local Peak Savitzky–Golay for Spatio-Temporal Reconstruction of Landsat NDVI Time Series: A Case Study Over the Qinghai–Tibet Plateau

Chenrun Sun, Zhaohui Xue, *Member, IEEE*, Ling Zhang, and Hongjun Su, *Senior Member, IEEE*

***Abstract*—The incompleteness of the normalized difference vegetation index (NDVI) time series (TS) restricts its expanded applications in key domains. Although spatio-temporal hybrid methods show promise in TS reconstruction, reliance on auxiliary data in most existing approaches introduces errors and increases workload. Furthermore, NDVI values marked as contaminated in the quality assessment (QA) data are underutilized. Ultimately, when utilizing spatial information, most methods are ineffective for the representation of land-use changes. Considering these issues, we propose a local peak Savitzky–Golay (LPSG) method for spatio-temporal reconstruction of Landsat NDVI TS. First, we construct a local peak neighborhood weighted interpolation (LPNWI) method that fully utilizes all original values to fill gaps. Second, we design a slope change decision tree (SC-DT) method for identifying residual noise, thereby mitigating the impact of QA errors on reconstruction results. Third, multidimensional calibration with weighted spatial reference (MDC-WSR) method is proposed to enhance utilization of spatial information by improving traditional correlation coefficient calculations and generating a multiyear spatial reference, which effectively reflects land-use changes. Experiments on Landsat NDVI TS data in the Qinghai–Tibet Plateau (2013–2022) show that: 1) LPSG outperforms other methods in mitigating the impact of QA errors, preserving TS peaks and details, and maintaining spatial continuity; 2) LPSG exhibits superior performance, with average RMSE reductions ranging from 0.00018 to 0.00750 compared to other methods under both correct and incorrect QA; and 3) LPSG demonstrates good robustness under various gap conditions and effectively restores TS of pixels affected by land-use changes.**

***Index Terms*—Landsat, normalized difference vegetation index (NDVI), Qinghai–Tibet plateau, Savitzky–Golay, spatio-temporal reconstruction.**

I. Introduction

NORMALIZED difference vegetation index (NDVI) time series (TS) derived from remote sensing images has been widely used in vegetation phenology detection [1], land-cover change monitoring [2], [3], [4]; environmental dynamic simulation [5], [6]; vegetation classification [7], etc. However, satellite remote sensing TS images are frequently interrupted due to low time resolution or pollution by bad atmosphere (such as aerosols and dust), clouds, and snow [8], [9]. Consequently, it becomes imperative to employ effective methods for reconstructing NDVI TS to meet the subsequent extended application. According to the principle of missing information restoration, three categories of NDVI TS reconstruction methods have been widely used in the past few decades, namely, temporal-based method, frequency-based method, and hybrid method.

1) *Temporal-based methods:* This category of methods can be further classified into three types. Temporal interpolation replacement methods, like iterative interpolation for data reconstruction (IDR) [10], the best index slope extraction (BISE) [11], and modified BISE (M-BISE) [12]. Temporal filter, including the Savitzky–Golay (SG) filter [13], Whittaker filtering method [14], and changing-weight (CW) filter [15]. Temporal function fitting methods, such as double logistic (DL) function fitting [16], and Fourier [17].

   The mentioned methods heavily rely on local temporal neighborhood information and have limited reconstruction capabilities. Consequently, researchers have extended temporal-based reconstruction methods. For instance, Liang et al. [18] utilized MODIS, Landsat8, and Sentinel-2 imagery at different spatio-temporal resolutions, employing gap-filling and Whittaker smooth filtering to recover NDVI TS. Yang et al. [19] enhanced the DCT-PLS method for reconstructing unevenly spaced data, generating high-quality and cloud-free Sentinel-2 NDVI TS.
2) *Frequency-based methods:* Frequency-based methods recover TS by transforming contaminated data from the time domain to the frequency domain. Notable methods in this category include the harmonic analysis of TS (HANTS) method [20], and the wavelet transform (WT) method [21]. However, these methods may unintentionally diminish reasonable high values and struggle to effectively preserve vegetation phenology. To address these limitations, improved frequency-based methods, such as the spatio-temporal prefill method with harmonic analysis of TS (ST-HANTS) [22], have been proposed.
3) *Hybrid methods:* The two aforementioned categories of methods have demonstrated success in specific

Manuscript received 14 April 2024; revised 4 June 2024; accepted 15 July 2024. Date of publication 23 July 2024; date of current version 5 August 2024. This work was supported in part by the National Natural Science Foundation of China under Grant 42271324 and Grant 42201406, and in part by the Natural Science Foundation of Jiangsu Province under Grant BK20221506. *(Corresponding author: Zhaohui Xue.)*

Chenrun Sun is with the School of Earth Sciences and Engineering, Hohai University, Nanjing 211100, China.

Zhaohui Xue and Hongjun Su are with the College of Geography and Remote Sensing, Hohai University, Nanjing 211100, China (e-mail: zhaohui.xue@hhu.edu.cn).

Ling Zhang is with the School of Naval Architecture & Intelligent Manufacturing, Jiangsu Maritime Institute, Nanjing 211170, China.

Digital Object Identifier 10.1109/JSTARS.2024.3432797

scenarios [23]. However, their extended application is limited due to the absence of consideration for spatial dimensions. In recent years, the hybrid methods that integrate both time and space information have garnered attention and research interest from scholars. Examples include the search and fill algorithm with moving offset method (SFA-MOM) [24], spatio-temporal Savitzky–Golay (STSG) method [25], and spatio-temporal tensor completion (ST-Tensor) method [26].

The current NDVI TS reconstruction methods encounter three primary challenges. First, existing methods are typically designed for MODIS NDVI products, characterized by coarse spatial resolution and high temporal resolution [27]. This raises concerns about the applicability of the algorithms to middle- and low-resolution images, posing challenges for TS reconstruction. Second, most methods are nonideal in scenarios involving long-term continuous data gaps. Third, a significant drawback is the heavy reliance on the pixel reliability index (RI) dataset in many existing methods, leading to substantial noise in reconstruction results when RI contains errors [26], [28].

For the first issue, Landsat and Sentinel NDVI TS data are suitable for more detailed applications. However, due to their higher spatial resolution and infrequent revisit frequency, reconstructing Landsat and Sentinel NDVI TS data is more challenging compared to coarser resolution data. Several studies have proposed novel reconstruction algorithms tailored to the intricate nature of these data. For instance, Yu et al. [29] proposed a climate incorporated gap-filling (CGF) method to generate Landsat NDVI TS at 8-day intervals. Chen et al. [30] obtained NDVI TS data by integrating MODIS NDVI TS data with cloud-free Landsat observations. Additionally, Yang et al. [31] proposed a method to synthetically generate gap-free NDVI TS from raw contamination observations for reconstructing Sentinel-2 NDVI TS. Landsat and Sentinel TS data have also been used for national- or local-scale mangrove species mapping [32], [33], mapping mangrove functional traits [34], sustainable mangrove management [35], coastal salt marsh mapping [36], which greatly benefits blue carbon research and precise management.

For the second issue, there are mainly two approaches to resolve it.

1) The first common approach involves using spatial neighboring pixels to reconstruct the NDVI value of the target pixel. Methods like STSG [25], ST-Tensor [26], wWHd [37], etc., have gained prominence in this context. Typically, these methods generate a 1-year reference NDVI TS to capture the seasonal growth pattern. This is accomplished by computing the average of all uncontaminated NDVI values for the corresponding day of the year (DOY) across all years in the TS. Subsequently, the correlation between the reference TS of neighboring pixels and the target pixel is calculated to identify similar pixels. Finally, the NDVI value from the generated spatial reference TS is directly utilized to replace the NDVI value labeled as a pollution point.
2) Another commonly employed approach is MODIS-Landsat spatio-temporal fusion for reconstructing Landsat NDVI TS data. Examples include the highly scalable temporal adaptive reflectance fusion model (HIST-ARFM) algorithm [38], GF-SG [30], enhanced gap-filling and Whittaker smoothing (EGF-WS) [18], and CGF [29]. Such methodologies typically require obtaining cloud-free Landsat and MODIS images simultaneously on the base date, as well as MODIS images for the prediction date, thus presenting certain limitations in their applicability.

For the third issue, a limited number of scholars have introduced new methods to mitigate the dependence on quality assessment (QA). For instance, Zhu et al. [39] proposed a reconstruction method based on self-weighting function fitting from curve features (SWCF) that does not require ancillary data about quality. Additionally, Yang et al. [40] proposed an enhanced STSG method (cuSTSG) that alleviates the impact of inaccurate quality marks on the final results.

While the aforementioned improved methods have addressed most of the problems to some extent, three shortcomings persist.

1) Most existing methods rely on other data sources as supplementary data of the same type (with strict fusion requirements) or on prior knowledge data, resulting in the introduction of additional errors and a substantial increase in both data volume and workload.
2) Few methods adequately utilize the NDVI points marked as contaminated points in QA, which may include both valid and invalid points. This inadequacy results in further scarcity of usable data and exacerbates the challenges associated with reconstruction.
3) In terms of using spatial information, the current methods mainly generate a 1-year reference TS using the same DOY, which results in the inability to represent land-use changes and may also cause the correlation coefficient between the neighborhood pixel and the target pixel to be falsely high, affecting the judgment of similar pixels.

To address the aforementioned issues, this study proposes a local peak Savitzky–Golay (LPSG) method for spatio-temporal reconstruction of Landsat NDVI TS based on two characteristics: TS variation of NDVI should be smooth and continuous, and the NDVI values are always subject to negative bias [10]. First, we construct a local peak neighborhood weighted interpolation (LPNWI) method to fill gaps, eliminating the need for auxiliary data and maximizing the utilization of all original values. Second, we design a slope change decision tree (SC-DT) method to detect residual noise and mitigate it using LPNWI, thereby minimizing the error impact of QA. Third, a multidimensional calibration with weighted spatial reference (MDC-WSR) method is proposed. To be specific, we design a new method to compute the weighted correlation coefficient between the target pixel and its neighborhood pixels, generating a 10-year weighted spatial reference (WSR), which effectively represents the land-use changes. Subsequently, positive and negative bias anomalies are detected and calibrated. Finally, the SG filter is applied to obtain a smooth and high-quality TS. The main contributions of this article are as follows.

1) We construct a new LPNWI method for gap filling that fully utilizes the dynamic change law of gradual local

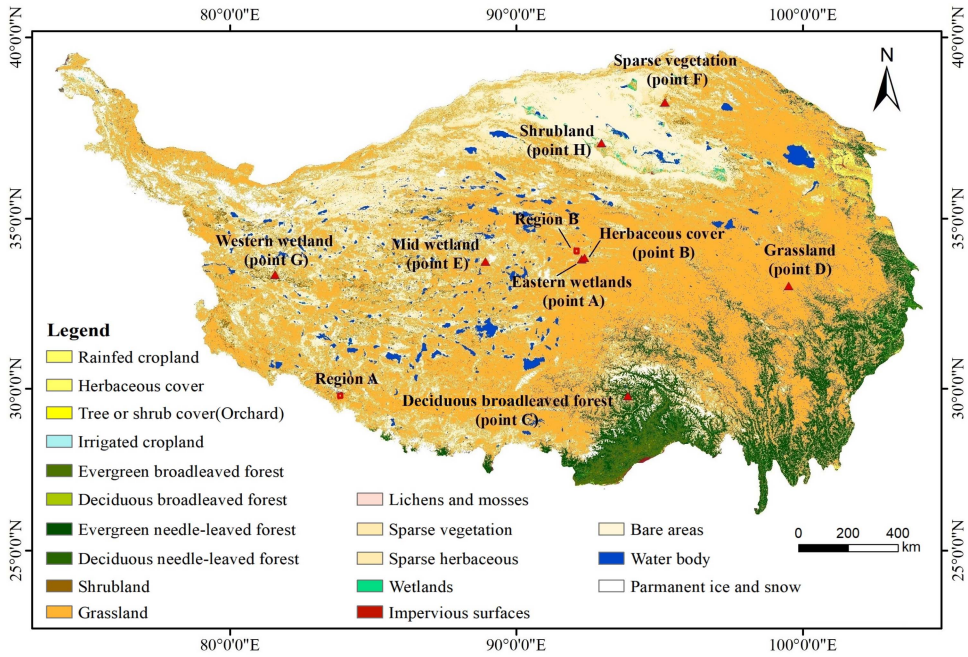

Fig. 1. Study area of Qinghai–Tibet Plateau with GLC_FCS30-2020 [42] as the base map covered by eight typical land-use types.

NDVI values and the characteristic that contaminated NDVI values tend to be negatively biased noise [10].

2) The SC-DT method designed to remove the noise present in TS after gap filling is well resistant to the uncertainty of QA quality.
3) The traditional method of calculating correlation coefficients between a target pixel and its neighborhood pixels is improved for generating WSR over multiple years, which is more robust in dealing with land-use changes and large long time gaps.

II. Study Area and Data

The Qinghai–Tibet Plateau (QTP) is situated in the southwest region of China, spanning from 25°–40°N and 74°–104°E, covering an area of roughly 2.5 million square kilometers [41]. With an average elevation surpassing 4500 m, this alpine ecoregion features various predominant vegetation types, including grassland, shrubland, and wetlands, as well as broadleaf and coniferous forests (refer to Fig. 1 for spatial distribution details). We collect surface reflectance data products of Landsat7 EMT+ and Landsat8-9 OLI from Google Earth Engine (GEE) and calculate NDVI using their red edge and near-infrared bands to test the reconstruction performance.

Meanwhile, this study generates a fused quality assessment (FQA) data based on QA of the original Landsat series data to accurately characterize pixel quality. Pixels affected by clouds, shadows, and snow/ice in the original Landsat series data are excluded. If the count of effective NDVI points is greater than or equal to 1, the NDVI value at that position is classified as reliable (FQA $= 1$); if there are no effective points, indicating noise in the NDVI value at that position (FQA $= 0$).

Finally, we utilize MOD09A1, MYD09A1, and MOD13Q1 products (retrieved from GEE) and Landsat series data to create a reference dataset (details are in Section IV-C). This reference dataset serves as the ground truth, enabling a quantitative evaluation of the reconstruction performance. Due to the lower spatial resolution of various MODIS products compared to Landsat, we upscale them on the GEE platform to standardize the spatial resolution of all data to 30 m. Specifics regarding the data used are presented in Table I.

III. Proposed Methodology

The flowchart of LPSG is shown in Fig. 2. First, gap-filling is performed on the original NDVI TS $\mathrm{T}_o \in \mathbb{R}^{1\times n}$ of points whose FQA are 0 using constructed LPNWI to generate the initially estimated NDVI TS $\mathrm{T}_e \in \mathbb{R}^{1\times n}$. Second, the proposed SC-DT is employed to identify residual noise, and LPNWI is applied again to fill them, resulting in the denoised NDVI TS $\mathrm{T}_d \in \mathbb{R}^{1\times n}$. Furthermore, the proposed MDC-WSR is utilized for TS calibration, generating the calibrated NDVI TS $\mathrm{T}_c \in \mathbb{R}^{1\times n}$. Finally, obtaining high-quality NDVI TS $\mathrm{T}_f \in \mathbb{R}^{1\times n}$ by applying the SG filter to smooth T_c. In this article, n denotes the number of points in the TS, and υ denotes the number of years.

A. LPNWI for Filling Gaps

The commonly used linear interpolation with filtering combination method [30] utilizes only the information of good NDVI values in adjacent time. However, when there is a long continuous gap, this method tends to obscure the original details of the TS. In this study, we propose LPNWI to fully consider all raw NDVI values as shown in Fig. 3.

In order to account for the scenario where the first or last points of TS are contaminated, we mirror the head and tail of the TS

TABLE I
DETAILS OF THE REMOTE SENSING DATA

Data	Name	Spatial-temporal resolution	Temporal range	Description
MODIS	MOD09A1	500m, 8-Day	2013.01–2022.12	Surface reflectance products of Terra MODIS
	MYD09A1	500m, 8-Day	2013.01–2022.12	Surface reflectance products of Aqua MODIS
	MOD13Q1	250m, 16-Day	2013.01–2022.12	Vegetation index (VI) products
Landsat	Landsat7 EMT+	30m, 16-Day	2013.01–2022.12	Level 2, Collection 2, Tier 1 surface reflectance
	Landsat8 OLI	30m, 16-Day	2013.01–2022.12	
	Landsat9 OLI	30m, 16-Day	2021.10–2022.12	

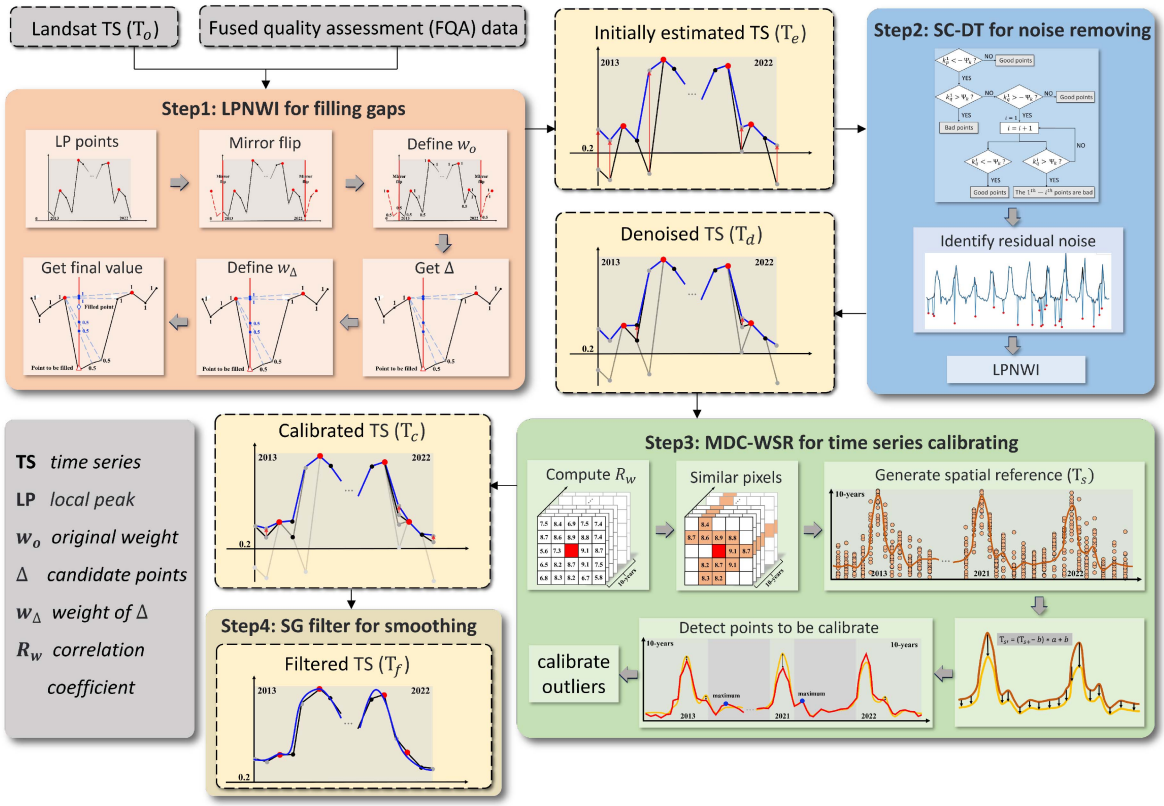

Fig. 2. Flowchart of the proposed LPSG method for spatio-temporal reconstruction of Landsat NDVI TS.

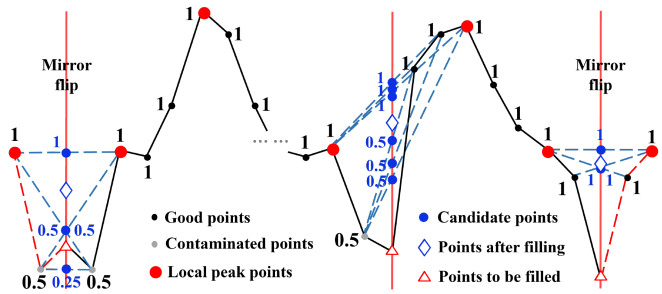

Fig. 3. Schematic of the proposed LPNWI method for filling gaps.

with a line parallel to the y-axis which represents the NDVI values. Specifically, the head represents all the points within the range from the first point of the TS to the first good point, and the tail represents all the points within the range from the last point to the last good point.

Above all, we define a local peak (LP) point as the point that is larger than the points on its left and right sides, and perform a weighted linear interpolation operation on every two adjacent LP points to fill the target value. In this regard, the original weight of each NDVI value $w_o \in \mathbb{R}^{1\times n}$ is determined according to the FQA. Specifically, when FQA is 1, the weight is set to 1; when FQA is 0, the corresponding weight is set to 0.5.

For each NDVI value to be filled T_o^m, the nearest uncontaminated LP points are identified to the left and right, forming left and right intervals containing ℓ and γ points, respectively. The ith point of the left interval and the jth point of the right interval are employed for linear interpolation to calculate the candidate value $\Delta^{(i,j)}$ for the target point. Finally, a weighted average is performed based on (1) to calculate the final filled NDVI value

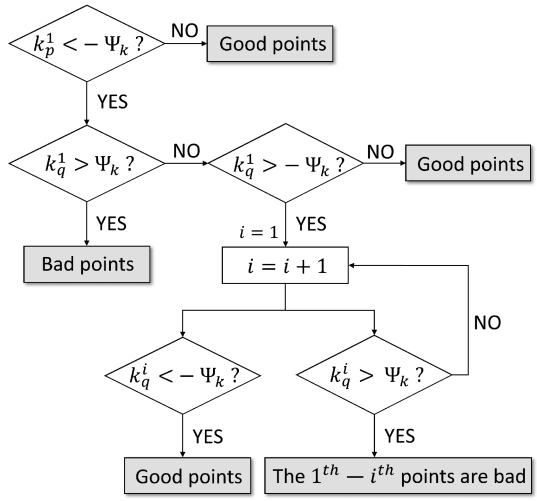

Fig. 4. Flowchart of the designed SC-DT method for identifying residual noise. "1th–ith" represents the first to ith point on the right side of the target point (including the target point).

T_e^m

$$\mathrm{T}_e^m = \sum_{i=1}^{\ell}\sum_{j=1}^{\gamma} w_{\Delta}^{(i,j)}\Delta^{(i,j)}$$
$$w_{\Delta}^{(i,j)} = \frac{w_o^{m-i} w_o^{m+j}}{\sum_{i=1}^{\ell}\sum_{j=1}^{\gamma} w_o^{m-i}\mathrm{T}_o^{m+j}} \quad (1)$$

where $w_{\Delta}^{(i,j)}$ is the weight of $\Delta^{(i,j)}$.

B. SC-DT for Residual Noise Removing

There could be errors in Landsat QA, potentially resulting in some contaminated NDVI points in FQA not being flagged, and there might be residual noise in T_e. Therefore, we design SC-DT, whose logic diagram is shown in Fig. 4 to identify residual noise.

We first compute the set of all slopes $k \in \mathbb{R}^{1\times(n-1)}$ in T_e, and the SC-DT also takes every two adjacent LP points as the unit of operation. In Fig. 4, k_p^i denotes the ith slope to the left of the target point within a pair of adjacent LP points, and k_q^j denotes the jth slope to the right of the target point within a pair of adjacent LP points. A smaller i indicates proximity to the target point. The formula for the slope threshold Ψ_k is provided in the following:

$$\Psi_k = \mathrm{sort}(|k|)\{2 \times \upsilon\} \quad (2)$$

where $\mathrm{sort}(|k|)$ is the sequence in which the absolute values of all slopes in the TS are arranged in descending order, and Ψ_k is the $(2 \times \upsilon)$th NDVI value in $\mathrm{sort}(|k|)$. It is assumed that there are at least two abrupt NDVI changes per year, namely, the presence of at least two slopes with larger absolute values.

Subsequently, we continue to use LPNWI (as described in Section III-A) to fill the detected residual noise. The only difference is that we adjust the weight of each point, as expressed

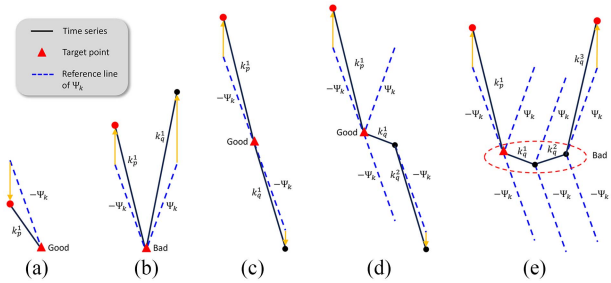

Fig. 5. Visualization of five scenarios in SC-DT noise detection process.

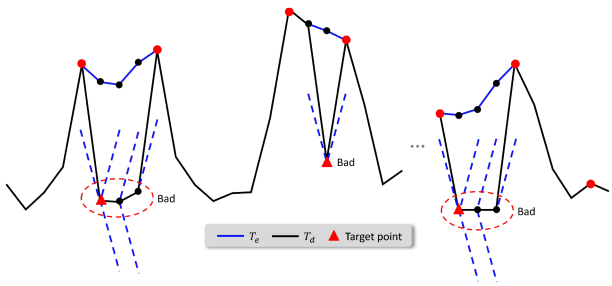

Fig. 6. Result diagram of SC-DT applied to TS.

in the following:

$$w_{o'}^m = \begin{cases} 1, & \mathrm{FQA} = 1 \text{ and } m \notin \mathrm{A} \\ 0.5, & \mathrm{FQA} = 1 \text{ and } m \in \mathrm{A} \\ 0.2, & \mathrm{FQA} = 0 \end{cases} \quad (3)$$

where A is the set of sequence numbers of the detected residual noise in the TS.

Fig. 5 visualizes five scenarios in the noise detection process using SC-DT. It is evident that identifying an instance as noise requires stringent criteria. Consequently, the slope threshold Ψ_k exhibits considerable tolerance, eliminating the necessity for parameter sensitivity experiments. Fig. 6 presents example results following the application of SC-DT to TS. Noise typically manifests as pronounced troughs between adjacent LP points, and the SC-DT method effectively identifies residual noise based on these LP points, restoring NDVI values to higher levels.

C. MDC-WSR for TS Calibrating

The previous steps involve gap-filling and denoising. However, relying solely on time dimension information may result in outliers, particularly when there is a continuous gap, leading to insufficient available time dimension information and an inability to restore the details of the vegetation growth curve. Adding spatial information can further correct the TS and ensure spatial continuity.

In this step, we construct MDC-WSR, which maximizes the utilization of NDVI values to calibrate the filled and denoised T_d. The generation process of WSR is illustrated in Fig. 7. Specifically, for the target TS T_d, the weight of all modified NDVI values is set to 0.5, while the remaining values are set to 1. As for the neighborhood TS $\mathrm{T}_n \in \mathbb{R}^{1\times n}$, only the good

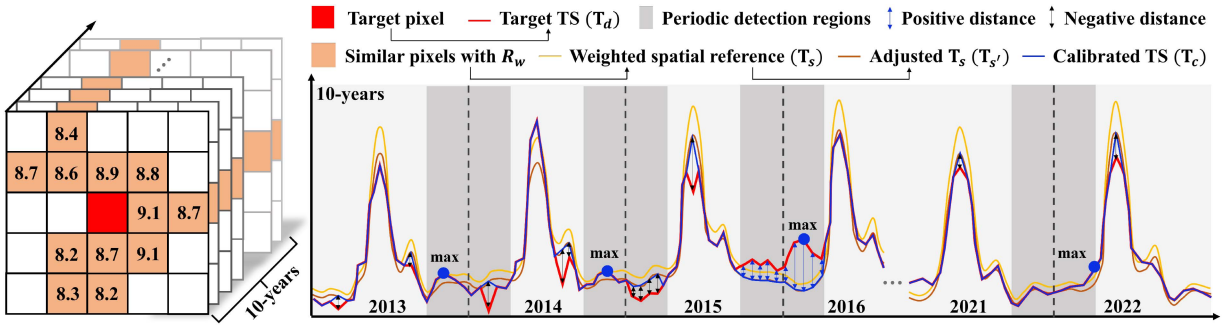

Fig. 7. Schematic of the proposed MDC-WSR method for TS calibrating.

points (FQA = 1) are taken into consideration. With the target pixel as the center, a neighborhood window with a half window (HW) length of 5 is created (when the NDVI value ratio of FQA = 0 is greater than or equal to 65%, HW is 10) to calculate the weighted correlation coefficient R_w of the target pixel and the neighborhood pixel, respectively, by (4). When R_w is greater than or equal to 0.76, the neighborhood pixel is determined to be a similar pixel. The determination process of above parameters is provided in Section IV-A

$$\begin{aligned} R_w &= \frac{\sum_{i=1}^{n} D_n^i D_d^i w_n^i w_d^i}{\sqrt{\sum_{i=1}^{n}(D_n^i w_n^i w_d^i)^2 \sum_{i=1}^{n}(D_d^i w_n^i w_d^i)^2}} \\ D_n^i &= \mathrm{T}_n^i - M_n \\ D_d^i &= \mathrm{T}_d^i - M_d \end{aligned} \tag{4}$$

where w_d^i and w_n^i represent the weights of the ith point in T_d and T_n, respectively. M_n is the average NDVI value remaining after removing contaminated points from T_n, and M_d is the average NDVI value remaining after removing modified NDVI values from T_d.

On each date, the contaminated points in the TS of all similar pixels are removed. Based on the R_w between the similar pixels and the target pixel, each similar pixel is assigned a corresponding weight. The weighted average is then calculated to obtain the NDVI value for that date. Any positions without a valid value are filled using linear interpolation. This process yields a preliminary WSR $\mathrm{T}_s \in \mathbb{R}^{1\times n}$. However, this spatial reference TS might only exhibit a similar shape to the TS of the central pixel and may not directly match in absolute position. This is because the TS associated with the central pixel TS may not necessarily align with the surface coverage of the central pixel, potentially being influenced by mixed pixels. Therefore, we perform translation and scaling operations on T_s to maximize its alignment with T_d, resulting in the final WSR $\mathrm{T}_{s'} \in \mathbb{R}^{1\times n}$

$$\begin{aligned} \mathrm{T}_{s'} &= (\mathrm{T}_{s+} - b) \times a + b \\ \mathrm{T}_{s+} &= \mathrm{T}_s + \mathrm{median}_{i\in[1,\upsilon]}\{\lambda_d^i - \lambda_s^i\} \\ b &= \mathrm{median}_{i\in[1,\upsilon]}\{\lambda_{s+}^i\} \\ a &= \mathrm{median}_{i\in[1,\upsilon]}\{(\varepsilon_d^i - b)/(\varepsilon_{s+}^i - b)\} \end{aligned} \tag{5}$$

where T_{s+} is the TS of T_s after an upward translation of $\mathrm{median}_{i\in[1,\upsilon]}\{\lambda_d^i - \lambda_s^i\}$ units, b is the baseline value of T_{s+}, and a is the scaling factor. λ_d^i and λ_s^i represent the NDVI value at the 20th percentile after arranging T_d and T_s in ascending order for the ith year. Additionally, ε_d^i represents the maximum value for the ith year of T_d, and median denotes taking the median.

Employing a certain percentage of data is effective in resisting the influence of outliers and enhancing data robustness [29], [43]. It is noteworthy that the 20th percentile rather than the minimum is utilized to mitigate the potential negative bias noise in the TS.

The preceding gap-filling and denoising operations have eliminated a significant portion of the noise in the TS. However, the NDVI values calculated based on LPNWI may not be entirely accurate. It may be due to the NDVI values between the adjacent LP points being too high, resulting in a high calculated fill value and a positive bias noise. In addition, SC-DT might overlook some subtle negative bias noise. Hence, we introduce spatial information to correct two categories of noise in T_d.

1) *Single point abnormal negative bias noise:* The difference of NDVI value between $\mathrm{T}_{s'}$ and T_d at each point D^m is calculated. When $D^m > \Psi_n$, T_d^m is considered as noise, and $\mathrm{T}_{s'}^m$ is used for calibration. The calculation of Ψ_n is provided in the following:

$$\Psi_n = M_D + R_n \times \mathrm{std}_D \tag{6}$$

where M_D and std_D refer to the mean and variance of all D after taking the absolute value, respectively. The determination process of parameter R_n is shown in Section IV-A.

2) *Continuous positive bias noise:* At the end of each year, a symmetrical time window with a HW length of 6 is created to check the low state of vegetation NDVI at the year transition. A total of $\upsilon - 1$ time windows are obtained, and the set of all window maxima is represented by $\mathrm{B} \in \mathbb{R}^{1\times(\upsilon-1)}$. Here, B^f denotes the fth maximum value. If $\mathrm{B}^f > \Psi_p$, then all NDVI values that have changed within this window are substituted with the corresponding values from $\mathrm{T}_{s'}$. Refer to the following for the calculation of Ψ_p:

$$\Psi_p = \mathrm{median}_{f\in[1,\upsilon-1]}\{\mathrm{B}^f\} + R_p \times \mathrm{std}_B \tag{7}$$

where std_B is the variance of B. For details on determining the parameter R_p, please refer to Section IV-A. The TS

after correction for single-point negative bias noise and continuous positive bias noise is denoted as T_c.

D. SG Filter for TS Smoothing

In the final step, we apply the SG filter, as defined in the following, to smooth the T_c, achieving a high-quality TS T_f with minimal noise:

$$\mathrm{T}_f^m = \left(\sum_{i=-s}^{s} C_i \mathrm{T}_c^{m+i} \right) / (2s+1) \tag{8}$$

where T_f^m is the mth value of T_f, C_i means the coefficient of the ith point in the sliding window, and s is the radius of the sliding window.

According to (8), the SG filter requires the manual selection of two parameters. First, the radius of the sliding window, where a larger radius results in a smoother reconstructed NDVI TS. Second, the order of the polynomial (typically 2–4), with lower orders leading to a smoother reconstructed NDVI TS. In this study, the SG filter parameters are configured with a window size of 5 and a polynomial order of 2.

The specific implementation process of LPSG is shown in Algorithm 1.

Algorithm 1: Local Peak Savitzky–Golay (LPSG).

Data: T_o and FQA
step1: LPNWI for filling gaps
$\mathrm{T}_e \leftarrow \mathrm{T}_o$;
$n \leftarrow length(\mathrm{T}_o)$;
the number of years υ;
determine w_o according to FQA;
for $i \in$ *where(FQA=0)* **do**
  compute T_e^i by Eq. 1
end
step2: SC-DT for residual noise removing
$\mathrm{T}_d \leftarrow \mathrm{T}_e$;
compute Ψ_k by Eq. 2;
obtain A by SC-DT;
compute $w_{o'}$ by Eq. 3;
for $i \in$ A **do**
  compute T_d^i by Eq. 1
end
step3: MDC-WSR for time series calibrating
$\mathrm{T}_c \leftarrow \mathrm{T}_d$;
for *all* T_n *in the* $4HW^2$ *neighborhood* **do**
  compute w_d and w_n;
  compute R_w by Eq. 4;
  if $R_w > 0.76$ **then**
    T_n is the similar TS
  end
end
compute T_s by weighted average according to R_w;
compute $\mathrm{T}_{s'}$ by Eq. 5;
compute Ψ_n by Eq. 6;
compute Ψ_p by Eq. 7;
determine the points to be adjusted and calibrate with $\mathrm{T}_{s'}$;
step4: SG filter for time series smoothing
$\mathrm{T}_f \leftarrow$ SG_filter(T_c);
Result: T_f

E. Quantitative Evaluation Indices

The root-mean-square error (RMSE) is used to evaluate the performance of the different methods. It is defined as

$$\mathrm{RMSE} = \frac{1}{n} \sqrt{\sum\nolimits_{i=1}^{n} \left(\mathrm{T}_{\text{predict}}^i - \mathrm{T}_{\text{true}}^i \right)^2} \tag{9}$$

where $\mathrm{T}_{\text{predict}}^i$ represents the ith value of the TS to be predicted, and $\mathrm{T}_{\text{true}}^i$ represents the ith value of the true TS.

IV. Experimental Results

In the experiment, we select two regions (500 × 500 pixels) and eight points of different land-use types within the QTP in China (see Fig. 1) to make the experiment more convincing. Four classical time filtering methods are selected for comparison with LPSG, i.e., the SG filter, the HANTS method, the Whittaker filter, and the Fourier algorithm. It is worth noting that before the time filtering, the time domain linear interpolation operation is first performed on the contaminated points (FQA = 0). The main difference between LPSG and the four comparison methods is that LPSG uses the newly proposed LPNWI to fill gaps and does not rely entirely on FQA to determine contaminated points. In contrast, the comparison methods use a linear interpolation method to fill in contaminated points that are entirely determined by FQA. Additionally, LPSG considers spatial information and inter-annual variations, which allows it to preserve the spatial correlation and temporal periodicity of TS data.

A. Parameter Sensitive Analysis

The LPSG method integrates the TS information of similar pixels in the neighborhood of the target pixel, which involves two key steps. The initial step of MDC-WSR involves retrieving similar pixels to generate WSR, which is crucial to determining the parameters of the neighborhood size and the correlation coefficient threshold. To establish the optimal values for these parameters, we conduct experiments using 400 random points in Region A (15 km × 15 km) and change the HW and correlation threshold under different proportions of random gaps. Analyzing Fig. 8, we observe that when the proportion of random gaps ranges from 10% to 60%, the optimal HW is 5; when the rate increases to 70%–80%, the optimal HW becomes 10. Additionally, when the correlation coefficient threshold is greater than or equal to 0.76, RMSE gradually increases. In summary, we determine that when the random gap rate of the target pixel is less than or equal to 65%, HW is set to 5, and when the rate exceeds 65%, HW is set to 10, with a correlation coefficient threshold of 0.76.

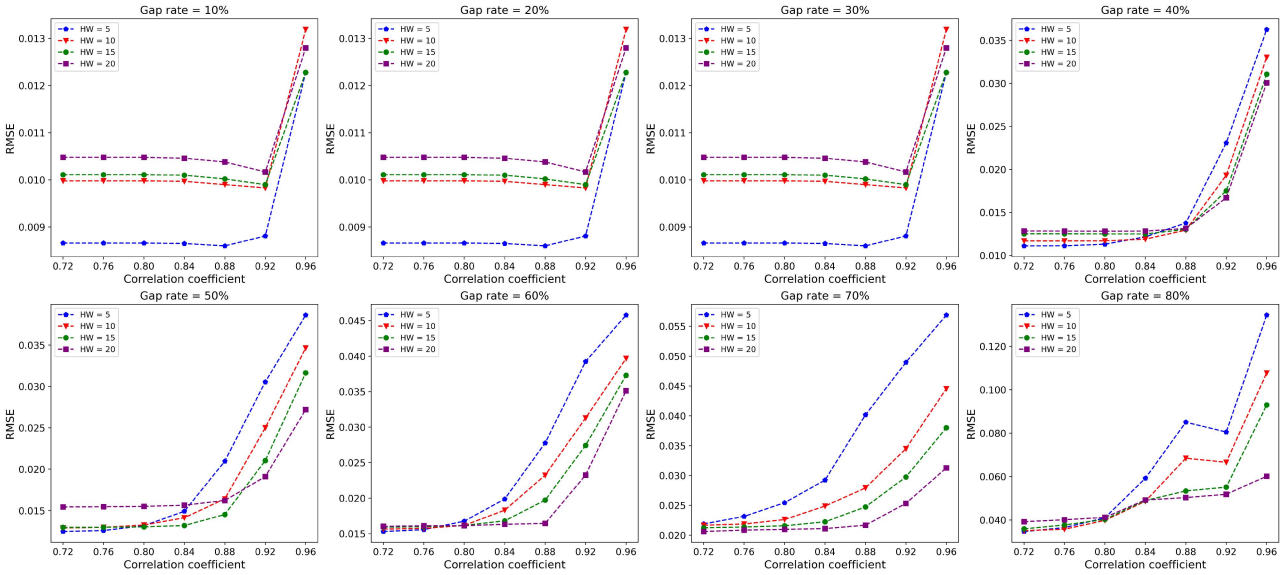

Fig. 8. Average RMSE of LPSG is calculated by changing only the HW size and the correlation coefficient threshold in the scenarios where the random gap changes from 10% to 80% with an interval of 10%. The simulation experiment is carried out on 400 random pixels of Region A.

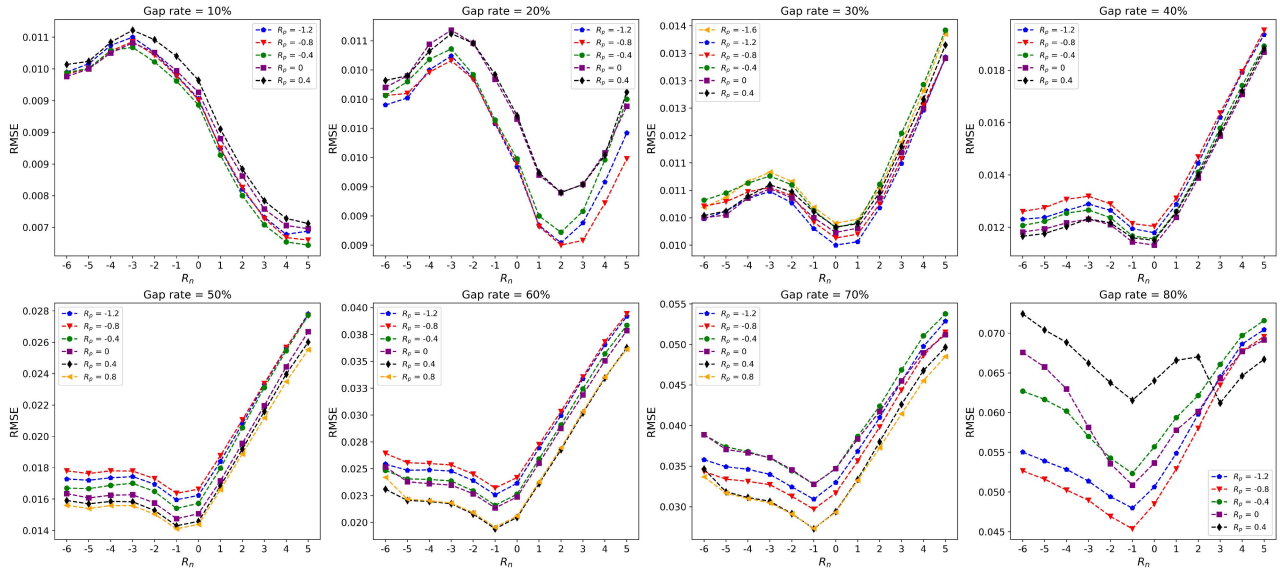

Fig. 9. Average RMSE of LPSG is calculated by only changing the positive bias correction threshold R_p and negative bias correction threshold R_n when the random gap changes from 10% to 80% with an interval of 10%. The simulation experiment is carried out on 400 random pixels of Region A.

The second step of MDC-WSR, involving determining the position to be calibrated from multiple dimensions and replacing it with the corresponding reference value, requires defining two parameters: the positive bias correction threshold R_p and the negative bias correction threshold R_n. These parameters are explored across various proportions of random gaps, as illustrated in Fig. 9. The observations indicate that, for R_p, the optimal effect is achieved within the 10%–30% gap rate range when the threshold is set to -0.8. At a 40% gap rate, the optimal threshold is 0, while for the gap rates ranging from 50% to 80%, the optimal threshold is 0.4. Regarding R_n, when the gap rate falls within the 10%–30% range, the average RMSE is minimized at values of 4, 2, and 0, respectively. Conversely, for gap rate between 40% and 80%, the optimal R_n is -1. The final values for both parameters are presented in the following formulas:

$$R_p = \begin{cases} -0.8, & R_{\text{gap}} < 35\% \text{or} R_{\text{gap}} > 80\% \\ 0, & 35\% \leqslant R_{\text{gap}} \leqslant 45\% \\ 0.4, & 45\% \leqslant R_{\text{gap}} \leqslant 80\% \end{cases} \tag{10}$$

$$R_n = \begin{cases} 2 \times (3 - 10 \times R_{\text{gap}}), & R_{\text{gap}} < 35\% \\ -1, & R_{\text{gap}} \geqslant 35\%. \end{cases} \tag{11}$$

TABLE II
GENERAL CHARACTERISTICS OF NDVI TS FOR EIGHT POINTS WITH DIFFERENT VEGETATION COVER TYPES

Vegetation cover type	Seasonal variation	Variation range of NDVI	Date of the maximum	Date of the minimum
Eastern wetland	Unconspicuous	0.05–0.15	July–August	November–April of the following year
Herbaceous cover	Obvious	0.10–0.35	July–August	November–April of the following year
Deciduous broadleaved forest	Obvious	0.20–0.80	July–August	December–March of the following year
Grassland	Obvious	0.20–0.60	July–August	November–April of the following year
Central wetland	Unconspicuous	0.05–0.10	July–August	November–April of the following year
Sparse vegetation	Unconspicuous	0.05–0.25	July–August	November–April of the following year
Western wetland	Unconspicuous	0.05–0.15	July–August	January–February of the following year
Shrubland	Obvious	0.10–0.35	July–August	February– April of the following year

B. Visual Evaluation of Reconstruction Results

1) Temporal Analysis: According to the GLC_FCS30 dataset [42], representative points of 8 different vegetation cover types are selected from southwest to northeast of the QTP, including eastern wetland (point A), herbaceous cover (point B), deciduous broadleaved forest (point C), grassland (point D), central wetland (point E), sparse vegetation (point F), western wetland (point G), and shrubland (point H). The results of different filtering methods are processed by 3-D curve expansion to visually compare the reconstruction effect. The general characteristics of NDVI TS for eight points with different vegetation cover types are shown in Table II.

Figs. 10 and 11 show the overall and local curves of the NDVI TS from 2013 to 2022 reconstructed by LPSG and the other four methods. Generally, LPSG retains the high value of NDVI and restores enough details in dealing with continuous noise and FQA errors. Specifically, the advantages of LPSG over other methods mainly reflect in four aspects.

1) LPSG better handles the false noise at the head and tail part of the TS, which may be significantly lower than the valley values of the same period in other years [e.g., the head and tail part of Figs. 10(a), (d), and 11(b)]. HANTS and Fourier methods underestimate the true NDVI value, while Whittaker and SG methods retain this false valley value. In contrast, LPSG efficiently identifies false valleys in the head and tail parts, and utilizes interannual information to accurately restore the values.
2) LPSG effectively avoids the influence of FQA errors. For some narrow and deep pseudovalleys in wetland and deciduous broadleaved forest [e.g., the years 2014, 2015, and 2020 in Fig. 11(a), the year 2015 in Fig. 10(b), the year 2014 in Fig. 11(c)], although the other four methods can filter these valleys to a certain extent, there are still obvious local troughs. LPSG successfully identifies abnormal abrupt NDVI values by SC-DT, ensuring they return to the correct values.
3) Compared to other methods, LPSG can better fill the continuous gaps. For example, in the latter half of 2016, there are continuous gaps at point D, and only LPSG restores TS to a shape similar to that of other years [see Fig. 11(b)]. Similar situations also appear in the transition between 2014 and 2015 in the central wetland point E [see Fig. 11(c)], 2019 in the sparse vegetation point F [see Fig. 11(d)], the connection between 2019 and 2020, and the connection between 2021 and 2022 in the western wetland point G [see Fig. 10(c)].
4) LPSG ensures the NDVI peaks of the original TS as much as possible. For example, in point A for the year 2018 [see Fig. 11(a)], in point E for the year 2016 [see Fig. 11(c)], and in point F for the year 2016 [see Fig. 11(d)]. One possible reason for the other four methods to underestimate the NDVI peaks is that the weights of each NDVI point are equal, and the fitting aims to place as many NDVI points as possible on the curve, resulting in the phenomenon of underestimating the peaks. Another possible reason is that other methods treat the possible false valley value near the peaks as the correct NDVI value, resulting in a sudden rise in the TS in a short time, and the peaks are determined as noise.

2) Spatial Analysis: Fig. 12 illustrates the comparison of Landsat NDVI TS data reconstructed by different methods across the entire QTP on the 8th day of 2020. In early January, the QTP is in winter, and the NDVI values of most vegetation are at a low level. However, due to factors such as cloud occlusion and satellite orbit, the original NDVI of vegetation in some areas is too low or even negative [especially in the striped dark area in Fig. 12(a)]. From the results, although the Whittaker, Fourier, HANTS, and SG methods improve the low value of the original data to a certain extent, the low value area of the strip is still obvious and the space is discontinuous. A large area of evergreen broadleaved forest is distributed in the southern part of the QTP, and this type of vegetation maintains active growth activities throughout the year, whose NDVI value in winter can generally be maintained at about 0.8. However, in the other four methods, Fourier increases the original NDVI value by the most, only increasing the value to about 0.4, while LPSG well restores the true high value of evergreen broadleaved forest and shows continuity and integrity in space. Fig. 13 illustrates the reconstruction results of different methods across the entire QTP on the 357th day of 2022. Evidently, as shown in Fig. 13(b) and 13(e), the reconstruction results of the HANTS and Fourier methods exhibit noticeable striping noise, failing to preserve the spatial continuity of the image. Fig. 13(c) and 13(d) demonstrates that the Whittaker and SG methods maintain spatial continuity relatively well, they fail to accurately recover the NDVI values for lake and river areas. The QTP is characterized

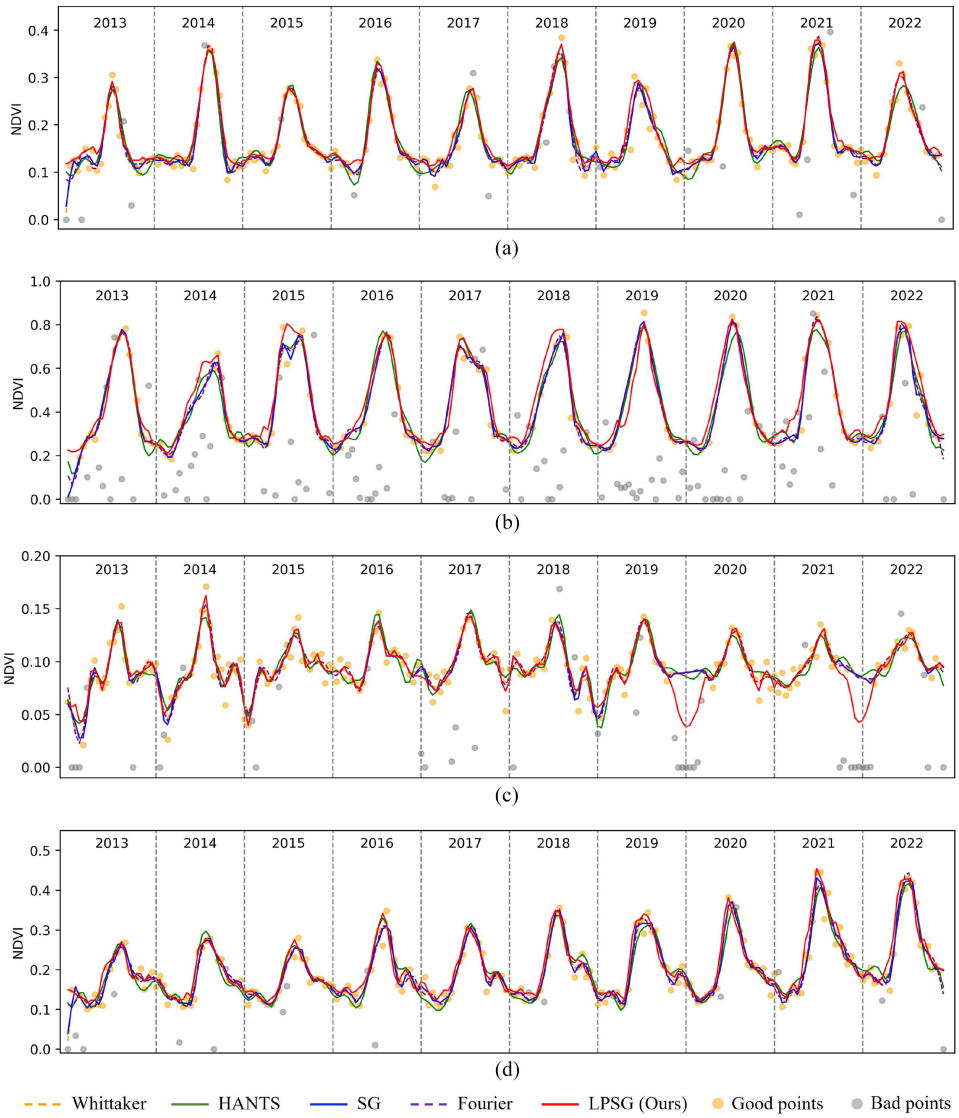

Fig. 10. Temporal reconstruction performance of different methods for some typical vegetation pixels. (a) Herbaceous cover (point B). (b) Deciduous broadleaved forest (point C). (c) Western wetland (point G). (d) Shrubland (point H).

by numerous lakes and extensive snow cover in its northern regions. Since water bodies and snow have lower reflectance in the near-infrared spectrum compared to the red spectrum, their NDVI values should be negative. The reconstruction results of the other four methods consistently overestimate the NDVI values in these areas, introducing high-value noise in regions where low NDVI values are expected. In contrast, the LPSG method effectively restores the NDVI values of water and snow-covered areas, presenting very clear low-value contours.

C. Index Evaluation of Reconstruction Results

To quantitatively evaluate the performance of LPSG, two regions located in the southwest (Region A) and middle (Region B) of the QTP are selected. Simulated data is reconstructed, and the average RMSE is calculated for each region. The simulated data are generated by adding noise to the true NDVI data based on actual pixel pollution. Since the NDVI true value of each pixel is unavailable, the reference data serves as the ground truth.

As depicted in Fig. 14, the NDVI data from MODIS and Landsat are amalgamated to synthesize NDVI values every 16 days. The final value of the reference data is determined by averaging when there are at least five uncontaminated good points. Conversely, linear interpolation is employed to calculate the corresponding reference NDVI value. The reference NDVI TS data generated through this method are independent at each time point, facilitating a more accurate restoration of the actual NDVI curve changes.

FQA is utilized in conjunction with the reference data to create simulation data for the experiment. Specifically, in locations where the NDVI point is contaminated (FQA $= 0$), a random negative noise of less than 40% is added to the reference NDVI value. If the NDVI value is of good quality (FQA $= 1$), it remains equal to the reference data. In practical scenarios, QA often

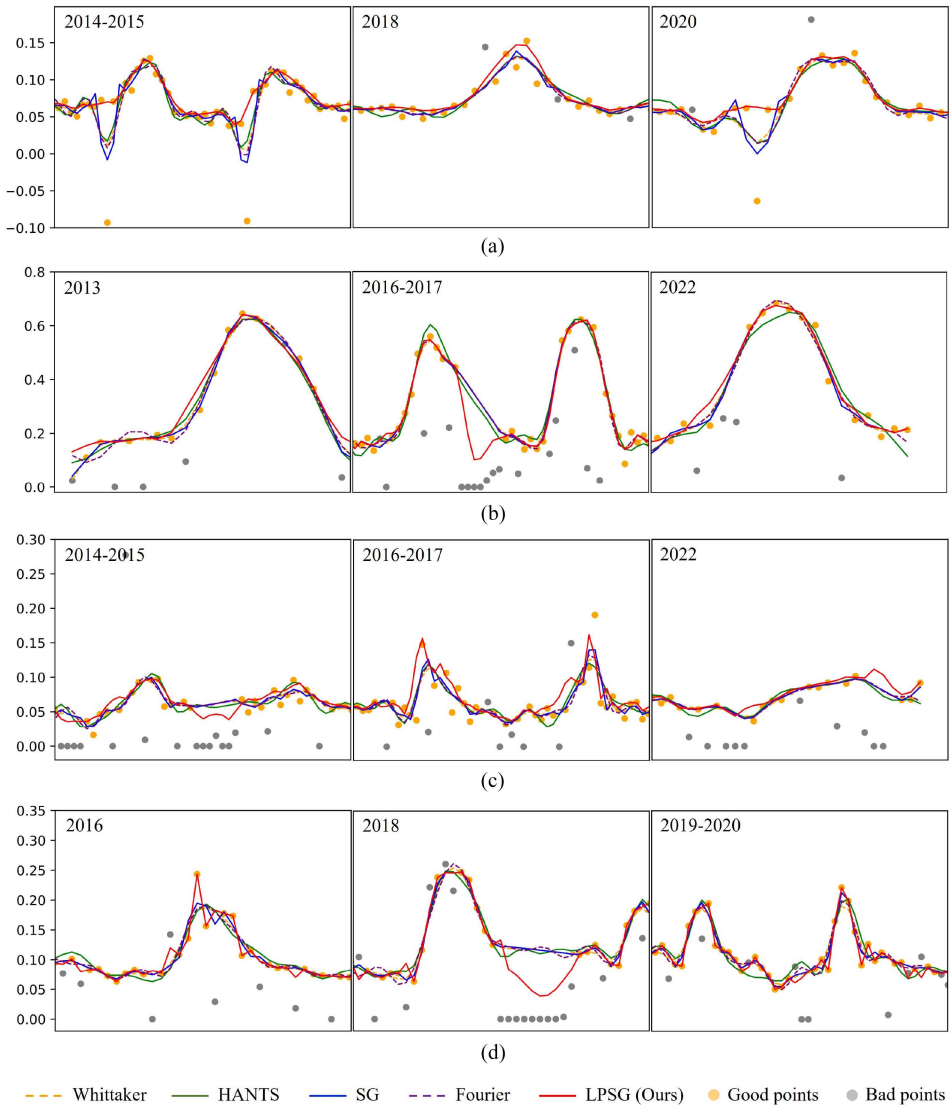

Fig. 11. Temporal reconstruction performance of different methods for some typical vegetation pixels (local zoom in). (a) Eastern wetland (point A). (b) Grassland (point D). (c) Central wetland (point E). (d) Sparse vegetation (point F).

encounters two situations: 1) marking good points as contaminated points and 2) marking contaminated points as good points. The former situation underestimates the number of available NDVI values with minimal impact, while the latter may mislead the TS with low details. Consequently, we evaluate the performance of LPSG in both cases of correct and incorrect FQA to demonstrate its robustness.

1) *Reconstruction of raw data with correct FQA:* Assuming the FQA is completely correct. Simulation data is generated based on the reference data for Region A and Region B, considering pollution in the original Landsat series data.
2) *Reconstruction of raw data with incorrect FQA:* The previous experiment simulated an ideal scenario, but reality may differ. In this experiment, we assume that 1% of the contaminated NDVI values in each pixel are labeled as good points (FQA = 1). Experiments are conducted separately in Regions A and B.

The results in Table III and Fig. 15 indicate the superior performance of LPSG, featuring the lowest RMSE and

TABLE III
MEAN RMSE VALUES OF DIFFERENT METHODS

Region	FQA	Whittaker	HANTS	Fourier	SG	LPSG (Ours)
A	✓	0.01286	0.01336	0.01187	0.01270	0.01169
	✗	0.01947	0.01970	0.01960	0.02132	0.01382
B	✓	0.01730	0.01791	0.01699	0.01598	0.01304
	✗	0.01969	0.02034	0.01994	0.01943	0.01498

Note: The symbol "✓" represents correct FQA, while "✗" denotes incorrect FQA.

the highest proportion of green regions in the images. Conversely, the Fourier and SG methods demonstrate comparatively inferior performance, while the Whittaker and HANTS methods exhibit relatively higher levels of efficacy. In Region A, when FQA is entirely accurate, the RMSE of LPSG is 0.00018 lower than the second smallest (Fourier) and 0.00167 lower than the largest (HANTS). In the presence of FQA

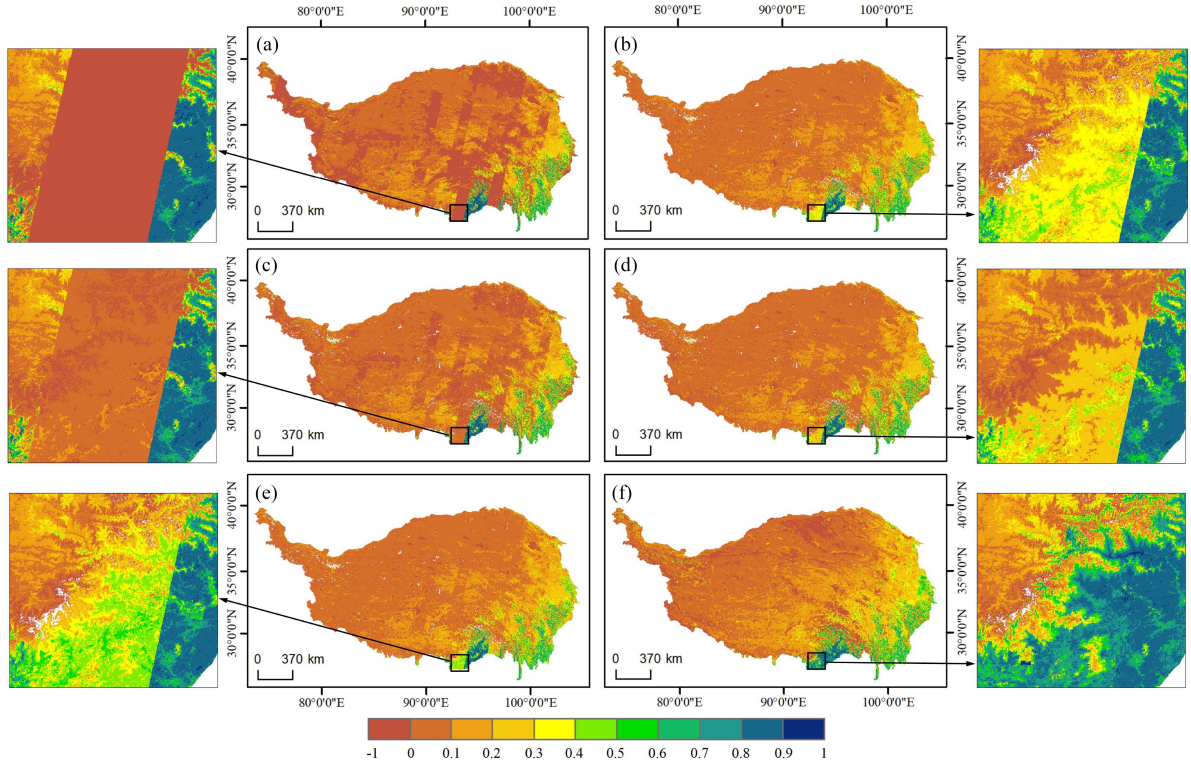

Fig. 12. Spatial reconstruction performance of different methods (taking the 8th day of 2020 as an example). (a) Raw NDVI. (b) HANTS. (c) Whittaker. (d) SG. (e) Fourier. (f) LPSG (Ours).

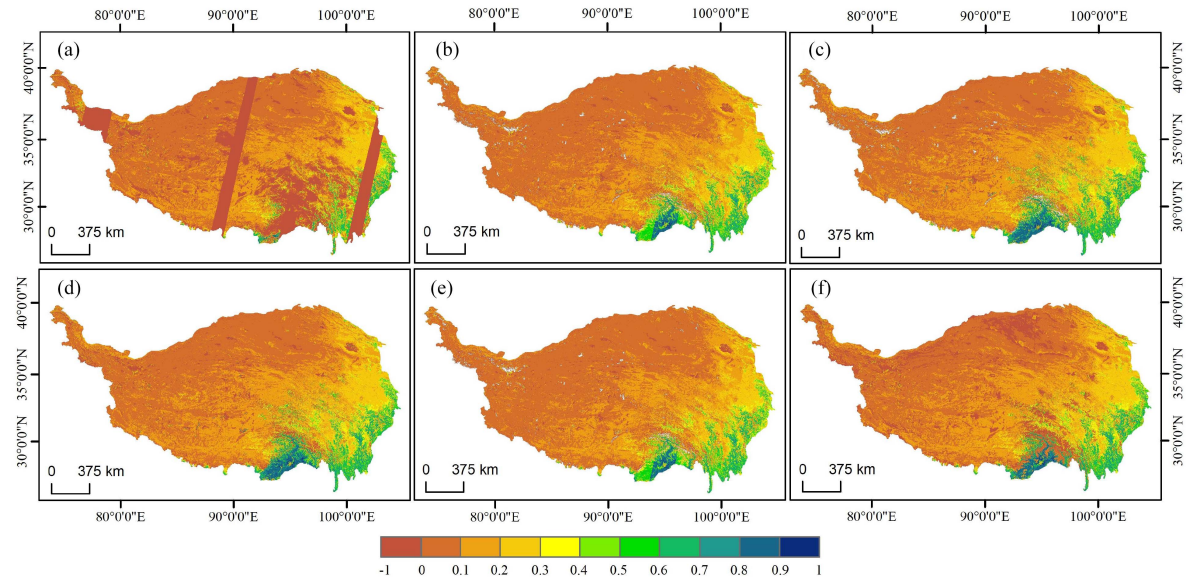

Fig. 13. Spatial reconstruction performance of different methods (taking the 357th day of 2022 as an example). (a) Raw NDVI. (b) HANTS. (c) Whittaker. (d) SG. (e) Fourier. (f) LPSG (Ours).

errors, the RMSE of LPSG is 0.00565 lower than the second smallest (Whittaker) and 0.0075 lower than the largest (SG). Shifting to Region B, under perfect FQA accuracy, the RMSE of LPSG is 0.00294–0.00487 lower than RMSE of other methods. In the presence of FQA errors, the RMSE of LPSG is 0.00445–0.00536 lower than the RMSE of other methods.

The spatial visualization images of different methods in Regions A and B are depicted in Fig. 16. Fig. 16(a) and 16(b) presents the reconstruction results of Region A on DOY 24 in 2013 and DOY 136 in 2016, mainly characterized by grassland, cropland, and deciduous broadleaved forest, heavily affected by clouds and snow contamination. While the other four methods are capable of rectifying the low values, notable negative bias

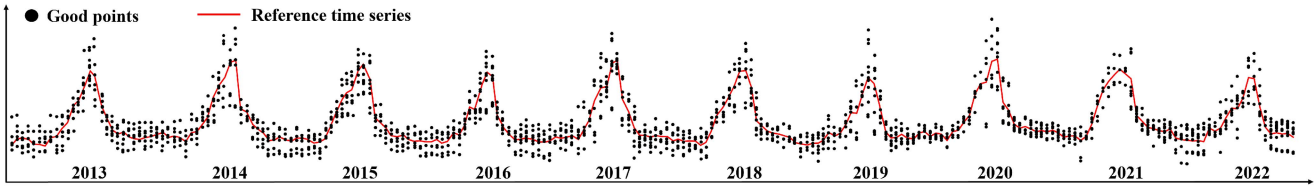

Fig. 14. Reference TS generated based on Landsat and MODIS data for evaluating reconstruction performance.

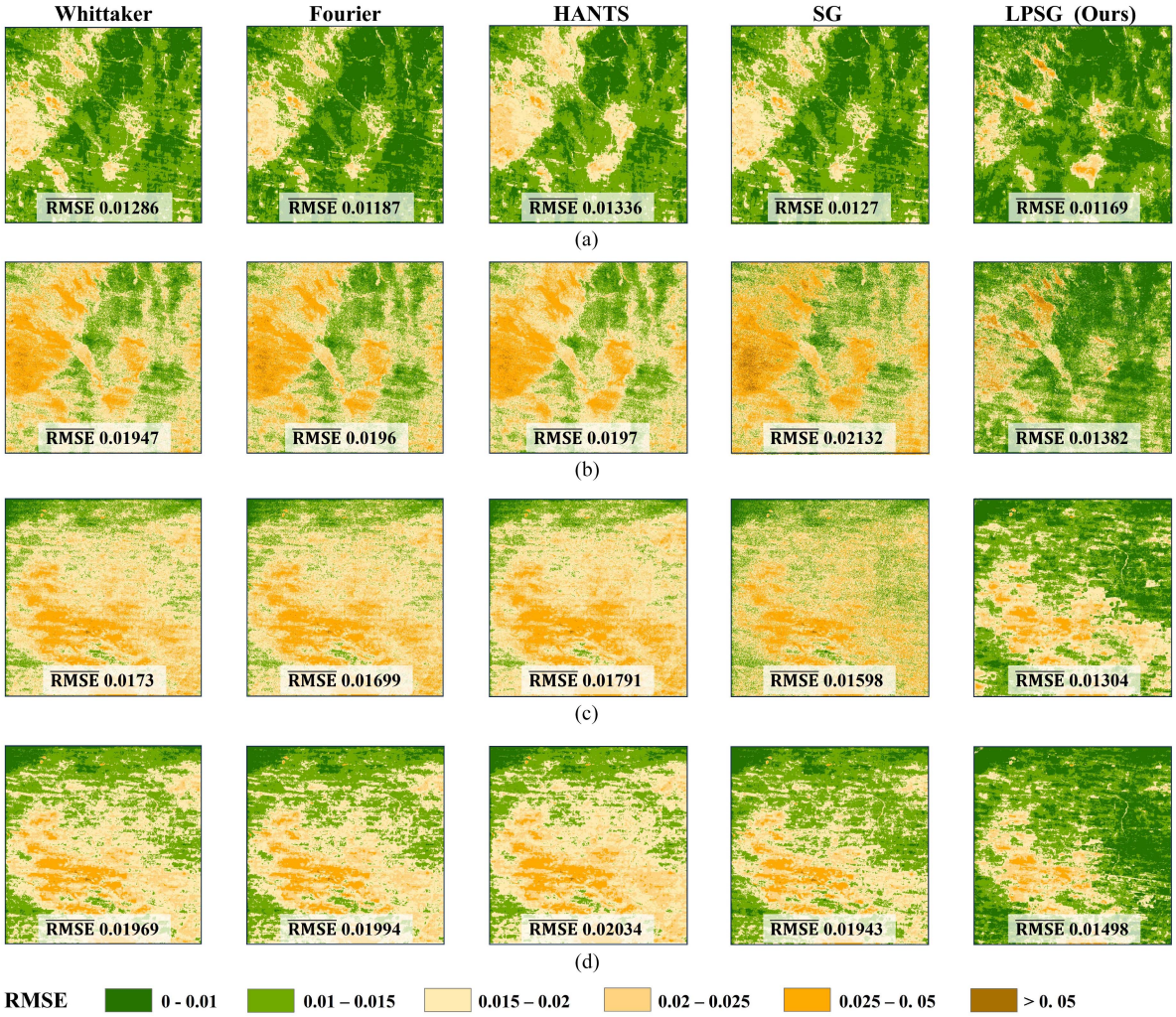

Fig. 15. RMSE visualization maps under conditions of correct FQA and incorrect FQA ($\overline{\text{RMSE}}$ denotes the spatial average RMSE). (a) Region A with correct FQA. (b) Region A with incorrect FQA. (c) Region B with correct FQA. (d) Region B with incorrect FQA.

noise is present in the results. Additionally, Fourier, SG, and HANTS methods introduce banded noise in their results. On the other hand, LPSG outperforms others in restoring high NDVI values and maintaining spatial continuity. Fig. 16(c) and 16(d) illustrates the reconstruction results of Region B, dominated by grassland and bare land, on DOY 73 in 2018 and DOY 40 in 2017. Although each method generally reconstructs NDVI values effectively, Whittaker, Fourier, HANTS, and SG methods produce significant salt and pepper noise with poor spatial continuity, while LPSG better ensures spatial correlation.

V. Discussions

A. Robust Analysis

Recent studies have highlighted the significance of filling missing values before fitting Landsat TS data [44]. The ability to fill missing values is a crucial criterion for assessing the performance of a reconstruction method. Therefore, it is essential to examine the stability of LPSG under different degrees of gaps. Given that this study retains contaminated NDVI value during the processing of the original data, and when the value does not

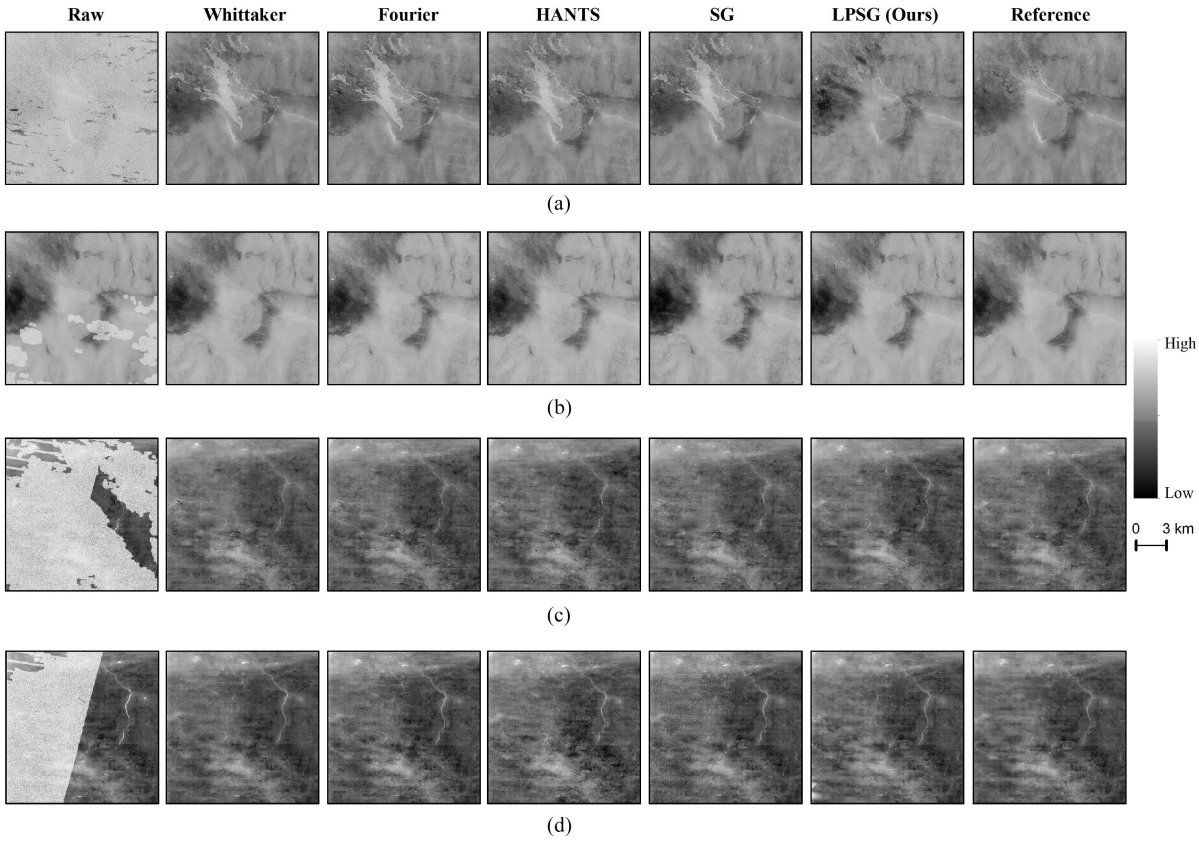

Fig. 16. Spatial reconstruction performance of different methods in Region A and Region B. (a) Region A with correct FQA on DOY 24 in 2013. (b) Region A with incorrect FQA on DOY 136 in 2016. (c) Region B with correct FQA on DOY 73 in 2018. (d) Region B with incorrect FQA on DOY 40 in 2017.

exist, it is set to 0, noise and gaps can be considered equivalent. We randomly select 400 pixels in Region A and simulate two types of noise based on the reference data.

1) *Case 1:* Random noise: For each pixel in the reference data, random noise ranging from 10% to 80%, with a 10% interval, is sequentially added in the time domain. The intensity of the noise is less than or equal to 40% of the reference value.
2) *Case 2:* Spatio-temporal continuous noise: A fixed 50 × 50-pixel rectangular patch, with a length ranging from 4 to 24 and a spacing of 2, is placed randomly within Region A, and noise is added to the NDVI values covered by the patch.

Fig. 17(a) illustrates the average RMSE of various methods under different proportions of random gaps. By comparing the changes in RMSE slopes, it is evident that LPSG exhibits superior reconstruction capabilities. Specifically, when the gap rate is below 20%, SG and LPSG demonstrate better performance. With the increases of the gap rate, the RMSE values of all methods also increase, but the distinction lies in the fact that the other four methods experience exponential growth, while LPSG exhibits linear growth with a small slope, especially when the gap rate is below 60%. Fig. 17(b) depicts the RMSE variation curve in the case of continuous spatio-temporal gaps. The RMSE curves of all five methods show a pattern of rising initially, followed by a decline, then another rise before stabilizing. The RMSE values of Fourier, Whittaker, and HANTS are higher and ultimately tend to converge. Additionally, although the SG method performs well when the gap length is less than or equal to 6, it sharply increases as the gap length grows, surpassing an RMSE value of 0.15. LPSG consistently maintains the lowest RMSE, and its change is the most gradual, with the RMSE remaining below 0.011.

B. Adaptability With Hybrid Land-Use

The LPSG is designed for reconstructing multiyear long TS. Therefore, a crucial consideration is whether the performance of the reconstruction method remains robust in the presence of land-use changes. In this experiment, we simulate two types of land-use changes based on the original data from Region A and Region B (see Fig. 18).

1) *Scenario 1:* Time dimension splicing. The first 5-year data (2013–2017) of Region A and the last 5-year data (2018–2022) of Region B are spliced to simulate land-use changes across all pixels.
2) *Scenario 2:* Spatial dimension splicing. The odd-columns data of Region A for the last five years are replaced with data from Region B at the corresponding positions, simulating land-use changes.

We use LPSG to compare the reconstructed TS with the spliced reference TS on the synthetic data. Fig. 19 primarily

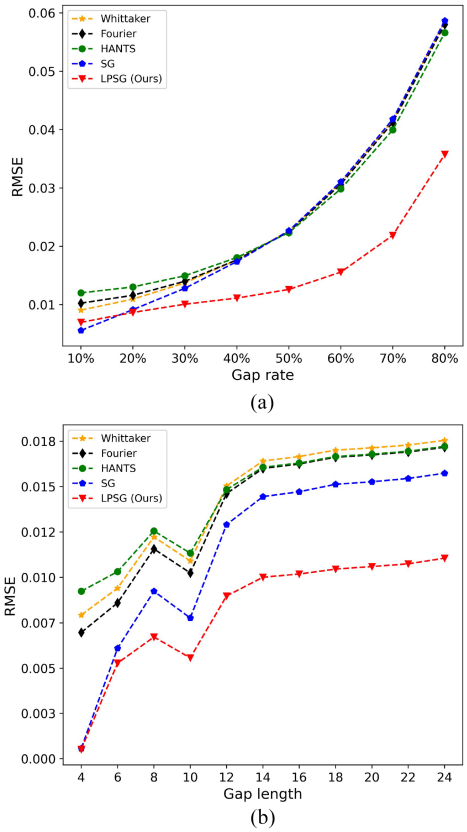

Fig. 17. Evolution of average RMSE obtained by different methods as a function of (a) gap rate and (b) gap length.

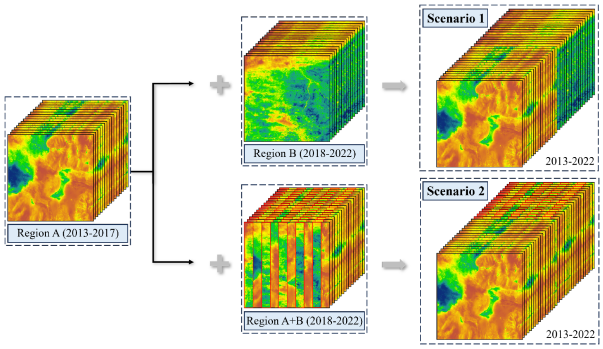

Fig. 18. Synthesis scenarios for 10-year NDVI TS data. In scenario 1, the first 5 years of Region A and the last 5 years of Region B are synthesized. In scenario 2, the odd-columns data represent land-use changes, while even-columns retain the original land-use of Region A.

illustrates the TS of land-use change from grassland to herbaceous vegetation. It is observed that the reference aligns well with the TS reconstructed by LPSG, demonstrating that LPSG is not sensitive to land-use changes, even if using multiyear periodic data. The explanation for this lies in the fact that, during the retrieval of information in the neighborhood of the target pixel, only pixels similar to the target pixel contribute to the calculation of WSR. In an extreme scenario, there might be no pixels similar to the target pixel in the surrounding area, and in such cases, LPSG does not utilize spatial information.

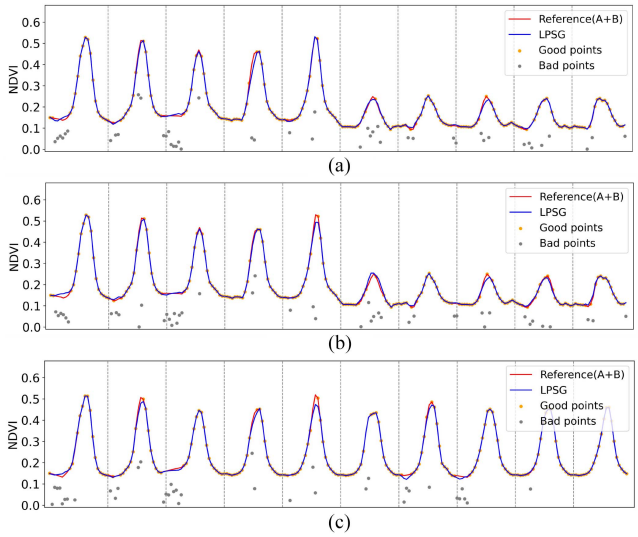

Fig. 19. Temporal reconstruction performance of LPSG under hybrid land-use. "Reference (A+B)" represents the concatenated reference data from Regions A and B. (a) Scenario 1. (b) Scenario 2 odd-columns. (c) Scenario 2 even-columns.

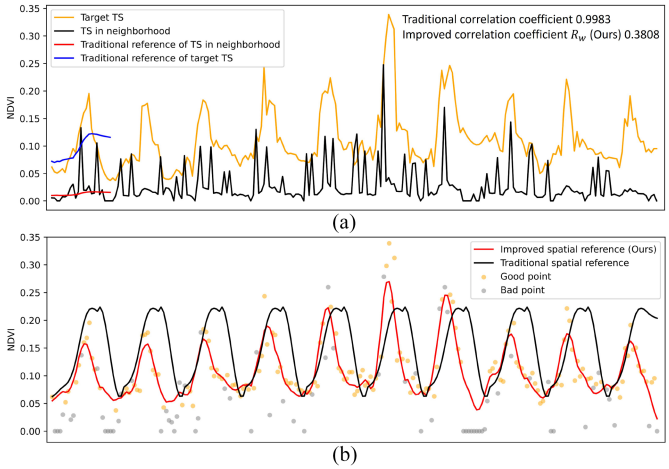

Fig. 20. Comparison of traditional and improved correlation coefficient and spatial reference. (a) Visualization of A TS in the target pixel neighborhood and the target TS. (b) Spatial reference results from both methods.

Previous studies have indicated that situations like these can be addressed by identifying land-use changes through continuous change detection and classification methods [45].

C. Validity Analysis of Improved Correlation Coefficient and Spatial Reference

To demonstrate the effectiveness of the improved correlation coefficient calculation method and spatial reference generation method in MDC-WSR (Section III-C), a random pixel is selected to visualize the correlation coefficient and spatial reference calculation processes using both methods. Fig. 20(a) illustrates the relationship between a TS within the neighborhood of the target pixel and the target TS. In traditional method, a spatial reference for each TS is generated prior to calculating the correlation coefficient by averaging the NDVI values for the same

day across different years. As a result, the traditional reference spans only one year. Visually, the two traditional references appear uncorrelated. However, due to their short length, the computed correlation coefficient is an unreasonably high 0.9983. In contrast, the improved method yields a correlation coefficient of 0.3808, more accurately reflecting the relationship between TS. Fig. 20(b) compares the spatial reference results from both methods. While the traditional spatial reference is smoother and exhibits clear periodic characteristics, its shape significantly diverges from the target TS and fails to capture interannual variations. Conversely, the improved spatial reference closely aligns with the target TS and effectively represents interannual changes. In conclusion, the improved correlation coefficient calculation method and spatial reference generation method in MDC-WSR are effective.

VI. Conclusion

Reconstructing Landsat NDVI TS data is crucial for meeting the demands of ecologically sensitive applications with medium to high spatial resolution. In this study, we develop LPSG, which does not rely on additional data and maximizes the utilization of all original data, including contaminated NDVI values. Additionally, we enhance the way in which spatial information is used in existing methods by generating a WSR of equal length to the original TS, considering both periodic and interannual variations.

The experimental results within the QTP region of China highlight the advantages of LPSG over four established methods (Whittaker, Fourier, HANTS, SG).

1) In both temporal and spatial dimensions, LPSG demonstrates the good ability to mitigate the impact of FQA errors, preserve peaks and local details of the TS, and maintain spatial continuity.
2) In terms of index evaluation, LPSG achieves a notable reduction in average RMSE compared to other methods, with decreases ranging from 0.00018 to 0.00750 in Region A and 0.00294 to 0.00536 in Region B under correct and incorrect FQA.
3) LPSG exhibits good robustness under different gap conditions and effectively restores the TS when the land-use changes in the study area.

Acknowledgment

The authors would like to thank the anonymous reviewers for their valuable feedback, which has contributed to improving the quality of the paper. Additionally, we extend our appreciation to the outstanding work and services provided by the Google Earth Engine team.

References

[1] L. Liu et al., "Detecting crop phenology from vegetation index time-series data by improved shape model fitting in each phenological stage," *Remote Sens. Environ.*, vol. 277, Aug. 2022, Art. no. 113060.

[2] X. Tang, E. L. Bullock, P. Olofsson, S. Estel, and C. E. Woodcock, "Near real-time monitoring of tropical forest disturbance: New algorithms and assessment framework," *Remote Sens. Environ.*, vol. 224, pp. 202–218, Apr. 2019.

[3] Y. Guan, Y. Zhou, B. He, X. Liu, H. Zhang, and S. Feng, "Improving land cover change detection and classification with BRDF correction and spatial feature extraction using Landsat time series: A case of urbanization in Tianjin, China," *IEEE J. Sel. Topics Appl. Earth Observ. Remote Sens.*, vol. 13, pp. 4166–4177, 2020.

[4] R. Zhang et al., "Tracking annual dynamics of mangrove forests in Mangrove National Nature Reserves of China based on time series Sentinel-2 imagery during 2016—2020," *Int. J. Appl. Earth Observ. Geoinform.*, vol. 112, Aug. 2022, Art. no. 102918.

[5] L. Tao, Y. Di, Y. Wang, and D. Ryu, "Normalized temperature drought index (NTDI) for soil moisture monitoring using MODIS and Landsat-8 data," *Remote Sens.*, vol. 15, no. 11, May 2023, Art. no. 2830.

[6] C. Qingkong, L. Erjun, C. Ju, L. Tao, and J. Ruibo, "Analysis on topographic effect of soil moisture in mountainous areas based on Landsat-8 OLI images," *J. Eng. Sci. Technol. Rev.*, vol. 13, no. 2, pp. 22–29, Apr. 2020.

[7] J. Luo et al., "A new technique for quantifying algal bloom, floating/emergent and submerged vegetation in eutrophic shallow lakes using Landsat imagery," *Remote Sens. Environ.*, vol. 287, no. 15, Mar. 2023, Art. no. 113480.

[8] R. Cao, Y. Chen, J. Chen, X. Zhu, and M. Shen, "Thick cloud removal in Landsat images based on autoregression of Landsat time-series data," *Remote Sens. Environ.*, vol. 249, Nov. 2020, Art. no. 112001.

[9] M. Wang et al., "Interannual changes of urban wetlands in China's major cities from 1985 to 2022," *ISPRS J. Photogrammetry Remote Sens.*, vol. 209, pp. 383–397, Mar. 2024.

[10] Y. Julien and J. A. Sobrino, "Comparison of cloud-reconstruction methods for time series of composite NDVI data," *Remote Sens. Environ.*, vol. 114, no. 3, pp. 618–625, Mar. 2010.

[11] M. Lange, B. Dechant, C. Rebmann, M. Vohland, M. Cuntz, and D. Doktor, "Validating MODIS and Sentinel-2 NDVI products at a temperate deciduous forest site using two independent ground-based sensors," *Sensors*, vol. 17, no. 8, Aug. 2017, Art. no. 1855.

[12] J. L. Lovell and R. D. Graetz, "Filtering pathfinder AVHRR land NDVI data for Australia," *Int. J. Remote Sens.*, vol. 22, no. 13, pp. 2649–2654, Nov. 2010.

[13] j. Chen, P. Jonsson, M. Tamura, Z. Gu, B. Matsushita, and L. Eklundh, "A simple method for reconstructing a high-quality NDVI time-series data set based on the Savitzky-Golay filter," *Remote Sens. Environ.*, vol. 91, no. 3-4, pp. 332–344, Jun. 2004.

[14] C. Atzberger and P. H. Eilers, "A time series for monitoring vegetation activity and phenology at 10-daily time steps covering large parts of South America," *Int. J. Digit. Earth*, vol. 4, no. 5, pp. 365–386, Jul. 2011.

[15] W. Zhu, Y. Pan, H. He, L. Wang, M. Mou, and J. Liu, "A changing-weight filter method for reconstructing a high-quality NDVI time series to preserve the integrity of vegetation phenology," *IEEE Trans. Geosci. Remote Sens.*, vol. 50, no. 4, pp. 1085–1094, Apr. 2012.

[16] P. S. A. Beck, C. Atzberger, K. A. Høgda, B. Johansen, and A. K. Skidmore, "Improved monitoring of vegetation dynamics at very high latitudes: A new method using MODIS NDVI," *Remote Sens. Environ.*, vol. 100, no. 3, pp. 321–334, Feb. 2006.

[17] M. E. Jakubauskas, D. R. Legates, and J. H. Kastens, "Harmonic analysis of time-series AVHRR NDVI data," *Photogrammetric Eng. Remote Sens.*, vol. 67, no. 4, pp. 461–470, Apr. 2001.

[18] J. Liang et al., "Using enhanced gap-filling and Whittaker smoothing to reconstruct high spatiotemporal resolution NDVI time series based on landsat 8, Sentinel-2, and MODIS imagery," *ISPRS Int. J. Geo-Inf.*, vol. 12, no. 6, May 2023, Art. no. 214.

[19] K. Yang, Y. Luo, M. Li, S. Zhong, Q. Liu, and X. Li, "Reconstruction of Sentinel-2 image time series using Google Earth Engine," *Remote Sens.*, vol. 14, no. 17, Sep. 2022, Art. no. 4395.

[20] J. Zhou, Li Jia, and M. Menenti, "Reconstruction of global MODIS NDVI time series: Performance of harmonic analysis of time series (HANTS)," *Remote Sens. Environ.*, vol. 163, pp. 217–228, Jun. 2015.

[21] L. Xiaoliang, L. Ronggao, L. Jiyuan, and L. Shunlin, "Removal of noise by wavelet method to generate high quality temporal data of terrestrial MODIS products," *Photogrammetric Eng. Remote Sens.*, vol. 73, no. 10, pp. 1129–1139, Oct. 2007.

[22] S. Li et al., "Monitoring vegetation dynamics (2010-2020) in Shengnongjia forestry district with cloud-removed MODIS NDVI series by a spatio-temporal reconstruction method," *Egypt. J. Remote Sens. Space Sci.*, vol. 26, no. 3, pp. 527–543, Dec. 2023.

[23] F. Xie and H. Fan, "Deriving drought indices from MODIS vegetation indices (NDVI/EVI) and land surface temperature (LST): Is data reconstruction necessary ?," *Int. J. Appl. Earth Observ. Geoinform.*, vol. 101, Sep. 2021, Art. no. 102352.

[24] S. K. Padhee and S. Dutta, "Spatio-temporal reconstruction of MODIS NDVI by regional land surface phenology and harmonic analysis of time-series," *GIScience Remote Sens.*, vol. 56, no. 8, pp. 1261–1288, Aug. 2019.
[25] R. Cao et al., "A simple method to improve the quality of NDVI time-series data by integrating spatiotemporal information with the Savitzky-Golay filter," *Remote Sens. Environ.*, vol. 217, pp. 244–257, Nov. 2018.
[26] D. Chu et al., "Long time-series NDVI reconstruction in cloud-prone regions via spatio-temporal tensor completion," *Remote Sens. Environ.*, vol. 264, Oct. 2021, Art. no. 112632.
[27] S. Li, L. Xu, Y. Jing, H. Yin, X. Li, and X. Guan, "High-quality vegetation index product generation: A review of NDVI time series reconstruction techniques," *Int. J. Appl. Earth Observ. Geoinform.*, vol. 105, Dec. 2021, Art. no. 102640.
[28] M. Claverie et al., "The harmonized Landsat and Sentinel-2 surface reflectance data set," *Remote Sens. Environ.*, vol. 219, pp. 145–161, Dec. 2018.
[29] W. Yu et al., "Gap filling for historical Landsat NDVI time series by integrating climate data," *Remote Sens.*, vol. 13, no. 3, Art. no. 484, Jan. 2021.
[30] Y. Chen, R. Cao, J. Chen, L. Liu, and B. Matsushita, "A practical approach to reconstruct high-quality landsat NDVI time-series data by gap filling and the Savitzky-Golay filter," *ISPRS J. Photogrammetry Remote Sens.*, vol. 180, pp. 174–190, Oct. 2021.
[31] Y. Yingpin, L. Jiancheng, H. Qiting, W. Wei, and S. Yingwei, "Weighted double-logistic function fitting method for reconstructing the high-quality Sentinel-2 NDVI time series data set," *Remote Sens.*, vol. 11, no. 20, Oct. 2019, Art. no. 2342.
[32] C. Zhao et al., "Mangrove species mapping in coastal China using synthesized Sentinel-2 high-separability images," *Remote Sens. Environ.*, vol. 307, 2024, Art. no. 114151.
[33] C. Zhao, M. Jia, Z. Wang, D. Mao, and Y. Wang, "Identifying mangroves through knowledge extracted from trained random forest models: An interpretable mangrove mapping approach (IMMA)," *ISPRS J. Photogrammetry Remote Sens.*, vol. 201, pp. 209–225, 2023.
[34] M. Jia et al., "Mapping mangrove functional traits from Sentinel-2 imagery based on hybrid models coupled with active learning strategies," *Int. J. Appl. Earth Observ. Geoinformation*, vol. 130, Jun. 2024, Art. no. 103905.
[35] C. Zhao et al., "Distribution of mangrove species Kandelia Obovata in China using time-series Sentinel-2 imagery for sustainable mangrove management," *J. Remote Sens.*, vol. 4, Apr. 2024, Art. no. 0143.
[36] C. Zhao, M. Jia, Z. Wang, D. Mao, and Y. Wang, "Toward a better understanding of coastal salt marsh mapping: A case from China using dual-temporal images," *Remote Sens. Environ.*, vol. 295, Sep. 2023, Art. no. 113664.
[37] D. Kong, Y. Zhang, X. Gu, and D. Wang, "A robust method for reconstructing global MODIS EVI time series on the Google Earth Engine," *ISPRS J. Photogrammetry Remote Sens.*, vol. 155, pp. 13–24, Sep. 2019.
[38] A. Moreno-Martínez et al., "Multispectral high resolution sensor fusion for smoothing and gap-filling in the cloud," *Remote Sens. Environ.*, vol. 247, no. 15, Sep. 2020, Art. no. 111901.
[39] W. Zhu, B. He, Z. Xie, C. Zhao, H. Zhuang, and P. Li, "Reconstruction of vegetation index time series based on self-weighting function fitting from curve features," *Remote Sens.*, vol. 14, no. 9, May 2022, Art. no. 2247.
[40] X. Yang, J. Chen, Q. Guan, H. Gao, and W. Xia, "Enhanced spatial–temporal Savitzky–Golay method for reconstructing high-quality NDVI time series: Reduced sensitivity to quality flags and improved computational efficiency," *IEEE Trans. Geosci. Remote Sens.*, vol. 60, 2022, Art. no. 4412317.
[41] R. Cao, Z. Xu, Y. Chen, J. Chen, and M. Shen, "Reconstructing high-spatiotemporal-resolution (30 m and 8-Days) NDVI time-series data for the Qinghai-Tibetan plateau from 2000–2020," *Remote Sens.*, vol. 14, no. 15, Jul. 2022, Art. no. 3648.
[42] X. Zhang, L. Liu, X. Chen, Y. Gao, S. Xie, and J. Mi, "GLC_FCS30: Global land-cover product with fine classification system at 30 m using time-series Landsat imagery," *Earth Syst. Sci. Data*, vol. 13, no. 6, pp. 2753–2776, Jun. 2021.
[43] A. Descals, A. Verger, G. Yin, and J. Penuelas, "A threshold method for robust and fast estimation of land-surface phenology using Google Earth Engine," *IEEE J. Sel. Topics Appl. Earth Observ. Remote Sens.*, vol. 14, pp. 601–606, Nov. 2021.
[44] L. Yan and D. P. Roy, "Spatially and temporally complete landsat reflectance time series modelling: The fill-and-fit approach," *Remote Sens. Environ.*, vol. 241, May 2020, Art. no. 111718.
[45] Z. Zhu and C. E. Woodcock, "Continuous change detection and classification of land cover using all available Landsat data," *Remote Sens. Environ.*, vol. 144, pp. 152–171, Mar. 2014.

Chenrun Sun received the B.S. degree in geomatics engineering in 2022 from Hohai University, Nanjing, China, where she is currently working toward the M.E. degree in remote sensing.

Her research interest includes wetland information extraction based on time series data.

Zhaohui Xue (Member, IEEE) received the B.S. degree in geomatics engineering from Shandong Agricultural University, Tai'an, China, in 2009, the M.E. degree in remote sensing from the China University of Mining and Technology, Beijing, China, in 2012, and the Ph.D. degree in cartography and geographic information system with Nanjing University, Nanjing, China, in 2015.

He is currently a Full Professor (Ph.D. supervisor) with the College of Geography and Remote Sensing, Hohai University, Nanjing. He has authored more than 60 scientific papers including more than 30 Science Citation Index (SCI) papers. His research interests include hyperspectral image classification, time-series image analysis, pattern recognition, and machine learning.

Dr. Xue was the recipient of the National Scholarship for Doctoral Graduate Students granted by the Ministry of Education of the People's Republic of China in 2014. He was awarded the Best Reviewer for the IEEE GEOSCIENCE AND REMOTE SENSING SOCIETY. He is an editorial board member in *National Remote Sensing Bulletin* (2020–2024). He has been a reviewer for more than ten famous remote sensing journals including IEEE TRANSACTIONS ON GEOSCIENCE AND REMOTE SENSING, *Remote Sensing of Environment*, and *ISPRS Journal of Photogrammetry and Remote Sensing*.

Ling Zhang received the B.S. degree in geomatics engineering from Shandong Agricultural University, Tai'an, China, in 2010, the M.E. degree in photogrammetry and remote sensing from the China University of Mining and Technology, Beijing, China, in 2013, and the Ph.D. degree in photogrammetry and remote sensing from Hohai University, Nanjing, China, in 2022.

Currently, she is an Associate Professor with the School of Naval Architecture and Intelligent Manufacturing, Jiangsu Maritime Institute, Nanjing. Her research interests mainly focus on machine-learning-driven soil moisture estimation using multisource remote sensing.

Hongjun Su (Senior Member, IEEE) received the Ph.D. degree in cartography and geography information system from the Key Laboratory of Virtual Geographic Environment (Ministry of Education), Nanjing Normal University, Nanjing, China, in 2011.

He is currently a Full Professor with the College of Geography and Remote Sensing, Hohai University, Nanjing. His main research interests include hyperspectral remote sensing dimensionality reduction, classification, and spectral unmixing.

Dr. Su was the recipient of the 2016 Best reviewer Award from the IEEE Geoscience and Remote Sensing Society. He is an Associate Editor of the *IEEE Journal of Selected Topics in Applied Earth Observations and Remote Sensing*.